GEOPHYSICS, VOL. 85, NO. 3 (MAY-JUNE 2020); P. MR155–MR166, 12 FIGS., 3 TABLES.
10.1190/GEO2018-0700.1

A viscoplastic model of creep in shale

Ehsan Haghighat[1], Fatemeh S. Rassouli[2], Mark D. Zoback[2], and Ruben Juanes[3]

ABSTRACT

We have developed a viscoplastic model that reproduces creep behavior and inelastic deformation of rock during loading-unloading cycles. We use a Perzyna-type description of viscous deformation that derives from a maximization of dissipated energy during plastic flow, in combination with a modified Cam-clay model of plastic deformation. The plastic flow model is of the associative type, and the viscous deformation is proportional to the ratio of driving stress and a material viscosity. Our model does not rely on any explicit time parameters; therefore, it is well-suited for standard and cyclic loading of materials. We validate the model with recent triaxial experiments of time-dependent deformation in clay-rich (Haynesville Formation) and carbonate-rich (Eagle Ford Formation) shale samples, and we find that the deformation during complex, multiscale loading-unloading paths can be reproduced accurately. We elucidate the role and physical meaning of each model parameter, and we infer their value from a gradient-descent minimization of the error between simulation and experimental data. This inference points to the large, and often unrecognized, uncertainty in the preconsolidation stress, which is key to reproducing the observed hysteresis in material deformation.

INTRODUCTION

Considering advances in observational tools, experiments, modeling methods, and computational resources, geologic models are becoming increasingly complex, taking into account nonlinear behavior and coupled phenomena (Settari and Mourits, 1998; Lewis et al., 2003; Thomas et al., 2003; Braun et al., 2008; Rutqvist et al., 2008; Segura and Carol, 2008; Aagaard et al., 2013; Jha and Juanes, 2014; Glerum et al., 2018). Rock deformation is responsible for a wide range of geologic processes such as compaction of reservoirs and subsequent changes in their performance, subsidence, stability of faults, and hydraulic fracturing. To better understand these processes and more accurately simulate them, the use of nonlinear mechanical models of rock is required. Although modeling of *elastic* time-dependent deformation (viscoelastic deformation) is a rather mature topic (Rundle and Jackson, 1977; Yang, 2000; Hagin and Zoback, 2004a, 2004b; Mavko and Saxena, 2016), modeling of *inelastic* time-dependent deformation is currently plagued with limitations. Inelastic time-dependent deformation in reservoir rocks, or creep, causes wellbore instability, changes to the hydraulic fracturing stimulation response, and changes in the state of stress in sedimentary basins at different time scales (Nakken et al., 1989; Leong and Chu, 2002; Sone and Zoback, 2013a, 2013b; Cao et al., 2014; Rassouli and Zoback, 2018). To accurately estimate the amount of subsidence, compaction, and change in the state of stress due to creep, this viscoplastic deformation should be included in geomechanical models (De Waal and Smits, 1988; Dudley et al., 1998; Tutuncu et al., 1998).

Because of its central importance to reservoir performance and fault behavior, creep in rocks has received increasing attention from an experimental standpoint (Amitrano and Helmstetter, 2006; Grgic and Amitrano, 2009; Heap et al., 2011; Sone and Zoback, 2013a, 2013b; Hao et al., 2014; Reber et al., 2014; Geng et al., 2017). Our recent series of short- and long-term cyclic creep experiments on clay- and carbonate-rich shales (Rassouli and Zoback, 2018) properly differentiates time independent from time-dependent deformation, allowing us to revisit viscoplastic modeling of rocks. However, in the proposed model, we do not consider viscoplastic effects that can possibly emanate from the pore fluid (e.g., Borja and Choo, 2016), or other deformation mechanisms due to chemical changes in the pore fluid, which can be important for clay-rich materials.

Modeling of viscoplastic deformations in soils and rocks has a long history (Finnie and Heller, 1959; Perzyna, 1966; Scholz, 1968;

Manuscript received by the Editor 17 October 2018; revised manuscript received 13 January 2020; published ahead of production 10 February 2020; published online 3 April 2020.
[1]Massachusetts Institute of Technology, Department of Civil and Environmental Engineering, Cambridge, Massachusetts, USA. E-mail: ehsanh@mit.edu.
[2]Stanford University, Department of Geophysics, Stanford, California, USA. E-mail: frasouli@stanford.edu; zoback@stanford.edu.
[3]Massachusetts Institute of Technology, Department of Civil and Environmental Engineering, Cambridge, Massachusetts, USA and Massachusetts Institute of Technology, Department of Earth, Atmospheric and Planetary Sciences, Cambridge, Massachusetts, USA. E-mail: juanes@mit.edu (corresponding author).

Borja and Kavazanjian, 1985; Wang et al., 1997; Dudley et al., 1998; Revil, 1999; Vermeer and Neher, 1999; Yang, 2002; Shao et al., 2003; Castelnau et al., 2008; Brantut et al., 2012). In early studies (Finnie and Heller, 1959; Scholz, 1968; Carter et al., 1981; Dudley et al., 1998), the viscoplastic deformation was modeled through an explicit time-dependent power-law function, intended to represent formation of microcracks in the rock (see also Borja and Kavazanjian, 1985). In many applications, such as creep modeling of sedimentary rocks, power-law models remain popular (Vermeer and Neher, 1999; Yin et al., 2010) and continue to be used to reproduce experimental curves (Sone and Zoback, 2014; Rassouli and Zoback, 2018). However, these models exhibit several deficiencies: (1) Explicit-time functional forms do not account for the dependence on the stress path, (2) they perform poorly for cyclic loading-unloading as the characteristic time changes, and (3) they lead to fundamental inconsistencies, such as stress relaxation inside the elastic domain.

To address these fundamental limitations of time-explicit models of creep, we propose and develop a *viscoplastic* model based on the concept of *overstress*, where the difference between the active applied stress and the preconsolidation stress (the maximum stress that the sample has experienced) is dissipated through a rate-dependent viscous flow (Perzyna, 1966). In particular, our model relies on modified Cam-clay (MCC) plasticity (Roscoe and Burland, 1968; Wood, 1990; Pietruszczak, 2010; Borja, 2013) and Perzyna-type viscoplasticity (Perzyna, 1966). Although Perzyna-type formulations have been previously used (e.g., Adachi and Oka, 1982; Kimoto et al., 2004; Chang and Zoback, 2010; Yin et al., 2010), these studies have used ad hoc functional forms of the viscoplastic multiplier. Instead, we derive it by imposing the principle of maximum plastic dissipation — also known as penalty regularization of dissipation energy (Simo and Hughes, 1998). We illustrate the performance of the new model by applying it to reproduce a series of experiments that we conducted on clay-rich and carbonate-rich shales (Rassouli and Zoback, 2018). The results show that the new viscoplastic model reproduces the short- and long-term cyclic loading paths exceptionally well, a feature that had heretofore remained elusive to constitutive modeling of creep.

VISCOPLASTIC MODEL

The volumetric response of geomaterials plays a significant role in their strength, and predicting it requires tracking the evolution of the void ratio (Coussy, 1995). This is expressed trivially in the small-deformation continuum kinematics, but it is less clear in the large-deformation range. In this section, we describe a new viscoplastic model under large volumetric changes. The model is developed within the class of Perzyna-type viscoplasticity models (Simo and Hughes, 1998), which ensures that it is thermodynamically consistent during viscoplastic evolution; i.e., the dissipated plastic energy during plastic flow remains positive (Lubliner, 1990; Pietruszczak, 2010).

Physically consistent volumetric decomposition in porous media

The kinematic relation for volume change in a continuum is described by

$$\frac{v}{V} = J \equiv \det(\mathbf{F}), \tag{1}$$

where V is the initial volume (reference configuration), v is the volume in the current (deformed) configuration, and $\mathbf{F}$ is the deformation gradient tensor (Truesdell and Toupin, 1960; Marsden and Hughes, 1983). In rate form, we can express

$$\dot{J} = J\,\mathrm{tr}(\mathbf{d}), \tag{2}$$

where $\mathbf{d} \equiv \mathrm{symm}(\nabla \mathbf{v})$ is the rate of deformation tensor and $\mathbf{v}$ is the (spatial) velocity field. Although the volumetric strain has traditionally been defined as

$$\varepsilon_v = \frac{v - V}{V}, \tag{3}$$

the proper definition in large deformations comes from integration of equation 2:

$$\varepsilon_v = \ln J = \ln \frac{v}{V}. \tag{4}$$

Under large inelastic deformation, the common decomposition of the volumetric deformation into its elastic and plastic parts is multiplicative, $J = J^e J^p$ (Simo and Hughes, 1998). It is unclear, however, how to relate these factors to the elastic and plastic evolution of the void ratio, which are physical, measurable quantities.

Here, we define a new volumetric decomposition that is consistent with physical definitions and can be directly related to geomechanical concepts. Any change in volume from the initial state will be decomposed into elastic and plastic parts. Therefore, the total volume in the final (deformed) configuration is expressed as $v = V + \Delta v^e + \Delta v^p$, or in rate form $\dot{v} = \dot{v}^e + \dot{v}^p$. Thus, we define the deformed elastic and plastic volumes as $v^\alpha = V + \Delta v^\alpha$, $\alpha = e, p$, so that

$$J = J^e + J^p - 1, \quad \text{where } J^\alpha = \frac{v^\alpha}{V}. \tag{5}$$

Note that the volumetric changes can then be evaluated as $\varepsilon_v = \ln J$, $\varepsilon_v^e = \ln J^e$, and $\varepsilon_v^p = \ln J^p$. Imposing the common geomechanical constraint of incompressibility of the solid grains relative to the voids, i.e., $v_s \approx V_s$ (Coussy, 1995), and recalling the definition of void ratio, $e = v_v/v_s$, we have $e^e = v_v^e/v_s$, and $e^p = v_v^p/v_s$, and we can then relate elastic and plastic parts of the void ratio to J for large volumetric changes:

$$e^e = (1 + e_0)J^e - 1, \qquad e^p = (1 + e_0)J^p - 1. \tag{6}$$

Although incompressibility of the grains is certainly only an approximation, it is defensible even for low-porosity media, especially in the regime of visco plastic deformations without localized failure. Indeed, ongoing experimental work on creep of shales using in situ X-ray techniques shows that most of the creep volumetric strains are a result of the change in the volume of the pores (Rassouli and Zoback, 2018).

The MCC model

Here, we adapt the classic MCC model to formulate the viscoplasticity framework (Roscoe and Burland, 1968; Borja, 2013). The MCC yield surface is described by the ellipse:

$$\mathcal{F}(\boldsymbol{\sigma}, \varepsilon_v^p) = \frac{q^2}{\eta_F^2} + p(p - p_y(\varepsilon_v^p)) = 0, \tag{7}$$

where $p = -(1/3)\mathrm{tr}(\boldsymbol{\sigma})$ is the volumetric stress (or "pressure") and $q = \sqrt{3/2\mathbf{s}:\mathbf{s}}$ is the von Mises stress, where $\mathbf{s} = \boldsymbol{\sigma} + p\mathbf{1}$ is the deviatoric stress ($\mathbf{1}$ is the unit tensor). The quantity p_y is the intercept of the elliptic yield surface with the p-axis (the center of the ellipse is located at $a \equiv p_y/2$) and η_F is the slope of the critical state line (CSL) in p-q space. According to this model, the evolution of the yield surface is a function of the plastic volumetric strain. Therefore, for the case of large volumetric changes, p_y needs to be modified to account for the kinematic relations involving the void ratio defined earlier.

Following the classic soil mechanics procedure of arriving at the evolution relations, we can express the void ratio changes as

$$de^e = -\kappa d(\ln\ p), \qquad de = -\lambda d(\ln\ p). \tag{8}$$

Substituting relation 6 into 8 and integrating, we obtain

$$p_y = p_{y0}\ \exp\left(\frac{1+e_0}{\lambda-\kappa}(1 - J^p)\right). \tag{9}$$

Note that in the classic expression for p_y, the term $1 - J^p$ is approximated as ε_v^p, which can be shown easily by a Taylor-series expansion.

Perzyna-type viscoplastic model

In Perzyna's model, the plastic viscous flow is related to the power of active stress (Perzyna, 1966). The active stress is defined as the distance between the current state of stress and the yield surface. Here, we adopt the principle of maximum plastic dissipation, by virtue of which we maximize the dissipation energy functional $\mathcal{D}_\mu^p$ (Simo and Hughes, 1998):

$$\underset{(\boldsymbol{\sigma},p)}{\mathrm{MAX}}\mathcal{D}_\mu^p[\boldsymbol{\sigma}^*, p^*; \dot{\boldsymbol{\varepsilon}}^p, \dot{\varepsilon}_v^p] := \boldsymbol{\sigma}^* : \dot{\boldsymbol{\varepsilon}}^p + p^*\dot{\varepsilon}_v^p - \frac{1}{2\mu}\langle\mathcal{F}(\boldsymbol{\sigma}^*, \varepsilon_v^p)\rangle^2. \tag{10}$$

Solving relation 10 results in the definition of viscoplastic strain rates:

$$\begin{aligned} \dot{\boldsymbol{\varepsilon}}^p &= \dot{\gamma}\frac{\mathbf{n}_\mathcal{F}}{|\mathbf{n}_\mathcal{F}|}, \quad \dot{\varepsilon}_v^p = \dot{\gamma}\frac{\mathcal{F}_{,p}}{|\mathbf{n}_\mathcal{F}|}, \quad \dot{\gamma} = \frac{\langle\mathcal{F}(\boldsymbol{\sigma}, \varepsilon_v^p)\rangle}{\mu(\varepsilon_v^p)p}, \\ \mathbf{n}_\mathcal{F} &= \frac{\partial\mathcal{F}}{\partial\boldsymbol{\sigma}}, \quad \mathcal{F}_{,p} = \frac{\partial\mathcal{F}}{\partial p}, \end{aligned} \tag{11}$$

where $\langle\cdot\rangle = \max(0, \cdot)$ denotes the Macaulay brackets. Equation 11 implies that viscous flow is proportional to the overstress, with a viscosity that depends on the plastic volumetric strain and acts as a hardening function. We take a simple exponential dependence

$$\mu(\varepsilon_v^p) = \mu_0\ \exp(\zeta\varepsilon_v^p), \tag{12}$$

which introduces two parameters (reference viscosity μ_0 and exponent coefficient ζ) and that, as we will see, leads to excellent quantitative agreement with the experimental data.

Elastic response

From equations 6 and 8, the volumetric response of the material can be expressed as

$$de^e \equiv (1 + e_0)dJ^e = -\kappa\frac{dp}{p}. \tag{13}$$

Expanding equation 13 and using the relations $\dot{J}^e = J\dot{\varepsilon}_v^e$ and $J = (1 + e)/(1 + e_0)$, we arrive at the volumetric stress-strain relation in the elastic domain:

$$dp = Kd\varepsilon_v^e$$

with

$$K = \frac{1+e}{\kappa}p, \tag{14}$$

where K is the bulk modulus, which is therefore pressure dependent. As a result, the elasticity tensor $\mathbb{D}$ is also pressure dependent, i.e., $\mathbb{D} \equiv \mathbb{D}(p)$. Our choice of a pressure-dependent elastic model is motivated by its ability to capture the nonlinear elastic behavior of geomaterials (Borja, 2013). Strictly speaking, however, this choice does not preserve elastic energy during cycles of loading-unloading (Zytynski et al., 1978). Preserving the elastic energy under cyclic loading would require the use of a hyperelastic model of elasticity (Houlsby, 1985; Borja et al., 1997). The use of hypoelasticity in the finite-deformation range also suffers from theoretical and computational issues regarding objectivity and frame invariance (for a detailed discussion, see section 7.3 of Simo and Hughes, 1998). Although this formulation has proven sufficient for modeling of our shale samples, it may need to be extended to use Jaumann objective rates for soft clayey soils undergoing significant volumetric deformation (Niemunis and Herle, 1997).

Summary and numerical implementation

At any given time step, the stress in the viscoplastic model is updated according to

$$\boldsymbol{\sigma} \equiv \boldsymbol{\sigma}_t + \mathbb{D} : \dot{\boldsymbol{\varepsilon}}^e\Delta t = \boldsymbol{\sigma}_t + \mathbb{D} : \Delta\boldsymbol{\varepsilon} - \mathbb{D} : \dot{\boldsymbol{\varepsilon}}^p\Delta t, \tag{15}$$

where all of the variables are evaluated at the current time step $t + \Delta t$ unless specifically described by a subscript of t. In equation 15, $\dot{\boldsymbol{\varepsilon}}^p$ is given in equation 11 with yield surface $\mathcal{F}(\boldsymbol{\sigma}, \varepsilon_v^p)$ given by the MCC model (equation 7). The quantity $\Delta\boldsymbol{\varepsilon}$ is the incremental strain, typically evaluated through finite-element nonlinear iterations. The nonlinear stress update is then implemented as a return-mapping algorithm (Simo and Ortiz, 1985; Simo and Hughes, 1998; Borja, 2013). As a result, the nonlinear strain residual takes the form $\mathbf{r} \equiv -\Delta\boldsymbol{\varepsilon} + \Delta\boldsymbol{\varepsilon}^e + \Delta\boldsymbol{\varepsilon}^p$, with $\Delta\boldsymbol{\varepsilon}^e = \mathbb{D}^{-1} : \Delta\boldsymbol{\sigma}$ and $\Delta\boldsymbol{\varepsilon}^p = \dot{\gamma}\Delta t\mathbf{n}_\mathcal{F}/|\mathbf{n}_\mathcal{F}|$, and the plastic multiplier is determined by rewriting $\dot{\gamma}$ in residual form: $\psi \equiv \mathcal{F}/p - \dot{\gamma}\mu(\varepsilon_v^p)$. The return-mapping algorithm is then a Newton iteration on variables $(\boldsymbol{\sigma}, \dot{\gamma})$:

$$\begin{aligned} \mathbf{r} + \frac{\partial\mathbf{r}}{\partial\boldsymbol{\sigma}} : \delta\boldsymbol{\sigma} + \frac{\partial\mathbf{r}}{\partial\dot{\gamma}}\delta\dot{\gamma} &= \mathbf{0}, \\ \psi + \frac{\partial\psi}{\partial\boldsymbol{\sigma}} : \delta\boldsymbol{\sigma} + \frac{\partial\psi}{\partial\dot{\gamma}}\delta\dot{\gamma} &= 0, \end{aligned} \tag{16}$$

where

$$\frac{\partial \mathbf{r}}{\partial \boldsymbol{\sigma}} = \mathbb{D}^{-1} + \partial_p \mathbb{D}^{-1} : \Delta\boldsymbol{\sigma} \frac{\partial p}{\partial \boldsymbol{\sigma}} + \dot{\gamma} \frac{\Delta t}{|\mathbf{n}_{\mathcal{F}}|} \left(\frac{\partial \mathbf{n}_{\mathcal{F}}}{\partial \boldsymbol{\sigma}} - \frac{1}{|\mathbf{n}_{\mathcal{F}}|} \mathbf{n}_{\mathcal{F}} \frac{\partial |\mathbf{n}_{\mathcal{F}}|}{\partial \boldsymbol{\sigma}} \right),$$
$$\frac{\partial \mathbf{r}}{\partial \dot{\gamma}} = \Delta t \frac{\mathbf{n}_{\mathcal{F}}}{|\mathbf{n}_{\mathcal{F}}|},$$
$$\frac{\partial \psi}{\partial \boldsymbol{\sigma}} = \frac{\mathbf{n}_{\mathcal{F}}}{p} - \frac{\mathcal{F}}{p^2} \frac{\partial p}{\partial \boldsymbol{\sigma}} - \dot{\gamma} \frac{\partial \mu}{\partial \varepsilon_v^p} \frac{\partial \varepsilon_v^p}{\partial \boldsymbol{\sigma}},$$
$$\frac{\partial \psi}{\partial \dot{\gamma}} = -\mu(\varepsilon_v^p) - \left(\frac{\partial p_y}{\partial \varepsilon_v^p} + \dot{\gamma} \frac{\partial \mu}{\partial \varepsilon_v^p} \right) \frac{\partial \varepsilon_v^p}{\partial \sigma_v}, \tag{17}$$

with the initial value of $\dot{\gamma} = \{F/p\}/\mu$. Solving the system of equation 16, the expressions for the updates are

$$\delta\dot{\gamma} = \frac{\psi - \partial_{\boldsymbol{\sigma}}\psi : \mathbb{E} : \mathbf{r}}{\partial_{\boldsymbol{\sigma}}\psi : \mathbb{E} : \partial_{\dot{\gamma}}\mathbf{r} - \partial_{\dot{\gamma}}\psi},$$
$$\delta\boldsymbol{\sigma} = -\mathbb{E} : (\mathbf{r} + \partial_{\dot{\gamma}}\mathbf{r}\delta\dot{\gamma}), \tag{18}$$

where $\mathbb{E}^{-1} = \partial_{\boldsymbol{\sigma}}\mathbf{r}$ and the normalization factor $|\mathbf{n}_{\mathcal{F}}|$ is given by $|\mathbf{n}_{\mathcal{F}}| = q^2/\eta_F^2 + p^2$. The consistent tangent operator takes the form

$$\mathbb{D}_T = \mathbb{E} - \frac{(\mathbb{E} : \mathbf{n}_{\mathcal{F}}) \otimes (\mathbf{n}_{\mathcal{F}} : \mathbb{E})}{\mathcal{H}_e - \mathcal{H}_p + \mathcal{H}_{vp}}, \tag{19}$$

where $\mathcal{H}_e = \mathbf{n}_{\mathcal{F}} : \mathbb{E} : \mathbf{n}_{\mathcal{F}}$, $\mathcal{H}_p = (\partial\mathcal{F}/\partial p_y) p_y'(\partial\mathcal{F}/\partial p)$, and $\mathcal{H}_{vp} = p((\mu/\Delta t)|\mathbf{n}_{\mathcal{F}}| + \dot{\gamma}\mu'(\partial\mathcal{F}/\partial p))$.

APPLICATION TO MODELING CREEP IN SHALE

To investigate the performance of the proposed model, we used the results of creep experiments conducted on four rock samples. The details of these experiments are given in Rassouli and Zoback (2018). Here, we present a brief summary of these creep laboratory tests, and we show that the new model reproduces the experimental observations accurately.

Experimental procedure

Experiments were conducted on two sets of shale samples: clay-rich samples from the Haynesville Formation in northwest Louisiana and East Texas, and carbonate-rich samples from the Eagle Ford Formation in South Texas. Each set contained two core plugs: one with parallel and the other with perpendicular bedding planes, oriented parallel to the axial loading axis. A summary of the characteristics and mineralogy of these samples is given in Table 1.

The creep experiments were performed in a triaxial loading apparatus following a cyclic pattern, with each cycle including four stages: loading, creep, unloading, and rebound. We loaded the samples to a certain value of deviatoric (differential) stress, kept the load constant so that the samples creep for a period of three to four hours, unloaded the sample to the minimum loading capacity of the triaxial system, and let the sample rebound for a similar time span as for the creep stage. These four loading steps were then repeated for 1 day, 1 week, and 4 weeks to study the effect of experimental time on the prediction of creep behavior of shale (Figure 1).

The confining pressure for all of the samples was 40 MPa during all the loading steps. The deviatoric stress for sample HV35 was increased to 30 MPa at the creep stages, whereas this value was equal to 40 MPa for all other samples. The applied load in the first cycle promotes closure of the microfractures initiated in the samples as a result of the changes in environmental conditions from the reservoir to the surface pressure and temperature.

Parameter identification

The initial void ratio of the sample is reported as $e_0 = 0.15$ (Rassouli and Zoback, 2018), and the Poisson's ratio is measured independently and taken as $\nu = 0.2$. The critical state parameter is assumed to be $\eta_F = 1.3$. Note that this parameter is not directly measured in the experiments — as the stresses stay well below the CSL — but it is taken within the range from different studies (Kutter and Sathialingam, 1992; Vermeer and Neher, 1999; Pietruszczak, 2010). These parameters are taken as known. Our first approach to identify the viscoplastic model parameters is to split them into two disjoint sets: yield-stress parameters and creep parameters.

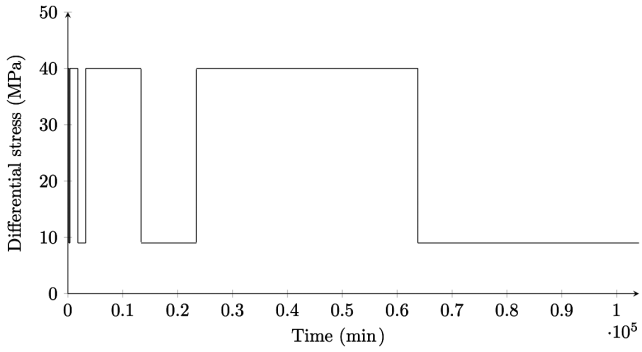

Figure 1. Time-cycling loading and unloading during the triaxial creep experiments. Shown here is the loading path for sample HV37, for which the differential stress for all the creep stages is equal to 40 MPa.

Table 1. Characteristics and mineralogy of the samples used for triaxial creep experiments, from Rassouli and Zoback (2018).

Sample	Formation	Orientation	Carbonate (wt%)	Clay (wt%)	TOC (wt%)	Water content (%)	Bulk density (g/cm^3)	Final porosity (%)
HV35	Haynesville	Vertical	7	62	1.6	1	2.47	8.1
HH37	Haynesville	Horizontal	7	62	1.6	1	2.47	8.1
EV8	Eagle Ford	Vertical	51.3	20	4.7	0.3	2.45	4.3
EH5	Eagle Ford	Horizontal	85.0	3	3.0	0.3	2.45	5.9

Yield-stress parameters

To define the yield stress relation (equation 9), we need to identify the parameters p_{y0}, κ, and λ. In a triaxial setup, these parameters can be inferred from the void ratio-effective pressure plots. The experimental data for sample HV35 (Figure 2) indicate an almost linear-elastic loading followed by time-dependent deformation at constant pressure. Therefore, while κ can be accurately evaluated from the unloading paths, this is difficult for p_{y0} and λ due to the lack of time-independent plastic deformation. Acknowledging this uncertainty, and using equation 9, the mean value for λ parameter is estimated as $\lambda = 0.0146$ from the loading paths. The mean value of κ from the unloading paths is evaluated as $\kappa = 0.0127$. The value of the ratio λ/κ is well outside the typical range (approximately 5–20), and thus we set $\lambda = 2\kappa$. Similarly, estimating the preconsolidation stress p_{y0} is not possible from the experimental *e-p* curve, again due to the lack of rate-independent inelastic deformation. From the nominal reservoir conditions for sample HV35 (50–75 MPa horizontal stress and 92 MPa vertical stress; Rassouli and Zoback, 2018), the equivalent preconsolidation stress is 64–80 MPa. However, the process of extreme decompression from reservoir to surface conditions can easily alter the microfabric of the rock, rendering the effective preconsolidation stress upon loading during the triaxial tests very different. Here, we use a value of $p_{y0} = 50$ MPa; otherwise, $\mathcal{F}$ would be very small and would not result in viscoplastic deformation. It is clear that these parameters are subject to large uncertainty due to lack of enough data in the plastic region. We will later show how a gradient-descent optimization approach can improve the estimation of these parameters.

Creep parameters

To evaluate the viscoplastic parameters, we analyze the time-dependent part of the deformation history. The viscosity function $\mu = \mu(\varepsilon_v^p)$ can be evaluated from equation 11. Rewriting this equation, we have

$$\mu = \frac{1}{\dot{\varepsilon}_v^p}\frac{\langle \mathcal{F}(\boldsymbol{\sigma}, \varepsilon_v^p)\rangle}{p}\frac{\partial_p \mathcal{F}}{|\mathbf{n}_{\mathcal{F}}|} = \frac{1}{\dot{\varepsilon}_v^p}\left\langle \frac{q^2}{\eta_F p} + (p - p_y(\varepsilon_v^p))\right\rangle (2p - p_y(\varepsilon_v^p)). \tag{20}$$

Because there is no direct measurement of $\dot{\varepsilon}_v^p$, we first perform a best fit on the ε_v^p data and then evaluate its time derivative. We assume a function of the form $\varepsilon_v^p = a\log(bt + c)$, which provides an excellent fit to the data (Figure 3a), and from which the time derivative is obtained $\dot{\varepsilon}_v^p = ab/(bt + c)$.

We now evaluate the plastic viscosity μ from the triaxial experiments via equation 20, and we perform curve fitting of the data with the exponential functional form in equation 12. This results in an excellent fit to the data, with parameter values $\mu_0 = 4.13 \times 10^6$ MPa s and $\zeta = 4.73 \times 10^3$ (Figure 3b).

Model predictions via 3D finite-element simulation

From the two-step procedure described in the previous section, we identified the following model parameters for the HV35 sample (Haynesville clay-rich shale): $\nu = 0.2$, $\eta_F = 1.29$, $\kappa = 0.0127$, $\lambda = 0.0254$, $p_{y0} = 50$ MPa, $\mu_0 = 4.13 \times 10^6$ MPa s, and $\zeta = 4.73 \times 10^3$. We are interested in determining the model predictions for this set of parameters and contrasting them with the actual measurements of axial strain during the multiscale, multicycle creep experiments.

Although it would be possible to do this by performing a single-degree-of-freedom calculation (in effect, a stress-driven integration of equation 15), we decided to implement the model in the finite-element code ABAQUS (Simulia, 2018) and reproduce the experimental conditions with a full 3D simulation with implicit time stepping that incorporates the time-varying boundary conditions of the triaxial setup (see Appendix A).

The result of the simulation is shown in Figure 4. It is apparent that the model can reproduce the time-dependent cyclic features of the creep experiment. Because this is done in the framework of viscoplasticity, the time-dependent deformation is stress driven and not

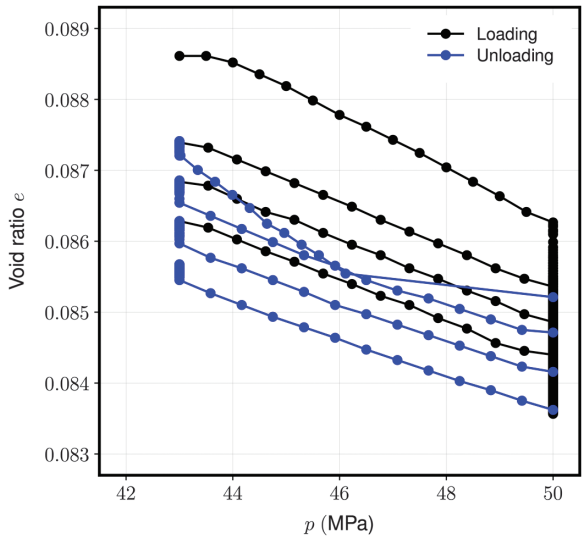

Figure 2. Evolution of void ratio e versus pressure p during all four loading-creep-unloading-rebound cycles, for sample HV35.

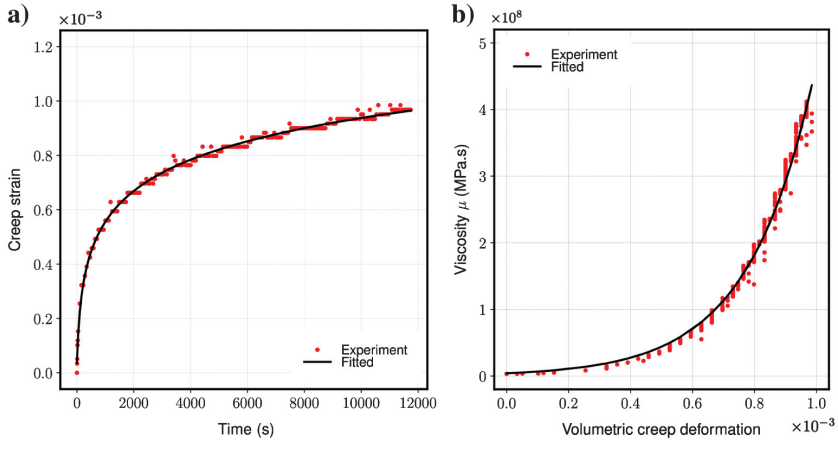

Figure 3. (a) Evolution of volumetric creep deformation ε_v^p versus time, with experimental data (the red points) fit by a logarithmic function (the black line). (b) Evolution of the plastic viscosity μ as a function of volumetric creep deformation ε_v^p, with data from the theoretical relation in equation 20 (the red points) fit by an exponential function (the black line). Data are for sample HV35.

controlled by an explicit relaxation-time parameter. We hypothesize that this is the reason why the response can be captured with a single set of parameters, despite the fact that the load-creep-unload-rebound cycles vary in duration from a few hours (the first cycle) to a few weeks (the fourth cycle).

Optimized parameter identification and model validation

In the previous section, we showed that the new viscoplastic model can reproduce the cyclic and time-dependent response of the creep deformation experiment. However, the simple procedure that we used for the parameter identification — separately for the yield stress parameters (κ, λ, and p_{y0} from the compression curve, Figure 2) and for the viscous deformation parameters (μ_0 and ζ from the creep deformation versus time curve, Figure 3) — means that the agreement between model predictions and experimental data is not quantitatively accurate (Figure 4).

To improve parameter identification, we use an iterative procedure that minimizes a cost function based on the L^2-norm of the mismatch between the measured ($\hat{\varepsilon}$) and simulated ($\varepsilon(\boldsymbol{\alpha})$) axial strain versus time:

$$I(\boldsymbol{\alpha}) \equiv \int_0^T (\varepsilon(t;\boldsymbol{\alpha}) - \hat{\varepsilon}(t))^2 dt, \tag{21}$$

where $\boldsymbol{\alpha} = (\kappa, \lambda, p_{y0}, \mu_0, \zeta)$ is the vector of parameters to be determined. Due to the short time periods of the cyclic loading at the start of the experiment, the use of actual time results in a better fit of the late times, whereas use of logarithmic time results in a better fit of the early times. Because we are particularly interested in the accurate evaluation of λ and p_{y0}, we use the expression in equation 21 as the cost function, with a logarithmic rescaling of time. We use a standard gradient-descent algorithm to perform the minimization, and we initialize the iteration using the two-step methodology described in the previous section. The result of the parameter identification for all four samples using this approach is reported in Table 2, and the performance of the model in reproducing the experimental data is shown in Figure 5. The results of the parameter optimization are relatively insensitive to the value of the critical-state parameter η_F (see Appendix A). In practice, the optimization algorithm would be applied to the pointwise stress evolution (at the "Gauss point level"). Given that it is a low-dimensional problem with only five parameters, the entire optimization procedure takes orders of magnitude less time and computational resources than a typical full-scale simulation for a real-world engineering problem.

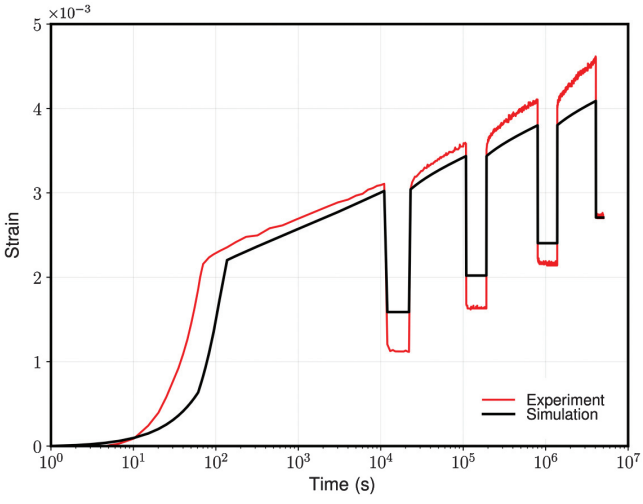

Figure 4. Comparison of axial strain from the laboratory experiment of sample HV35 (red) and the 3D finite-element simulation with implicit time integration of our viscoplastic model (black), with the initial identification of model parameters.

DISCUSSION

Figure 5 clearly shows that the proposed viscoplastic model of creep provides an excellent quantitative agreement with the deformation behavior of shale measured in triaxial experiments. The obvious disparity between model and experiments for the EH5 sample is due to a read-out issue in the strain gauge after the first loading cycle.

The model exhibits the remarkable ability to capture the deformation behavior for multistaged, multiscale loading cycles (note the logarithmic scale of the time axis in Figure 5). This central feature of the model is the result of the overstress-driven formulation (Perzyna, 1966; Simo and Hughes, 1998), and it sets our model apart from existing models of creep (Finnie and Heller, 1959; Scholz, 1968; Carter et al., 1981; Dudley et al., 1998; Vermeer and Neher, 1999; Yin et al., 2010), which use a time-explicit viscoplastic function — something that requires setting a characteristic time for stress relaxation, which, by definition, prevents capturing the material's time-dependent deformation under disparate periods of creep between loading and unloading (Sone and Zoback, 2014; Rassouli and Zoback, 2018).

When using the optimized model parameters in Table 2, the model improves the fit to the data significantly with respect to the initial parameters (compare Figures 4 and 5 for HV35). In this particular case, the improvement in model performance can be attributed to the refined identification of parameters κ and p_{y0}. An interesting and nonintuitive outcome from our analysis is that the preconsolidation stress p_{y0} should be understood as a fitting parameter in our model (and probably in other soil- and rock-mechanics models), when the samples are subject to unconstrained decompression from reservoir conditions, likely generating microfractures and altering the fabric of the rock.

The model parameters all have a physical interpretation. This is illustrated directly by analyzing the sensitivity to each parameter around the optimum (Appendix A). It is informative to analyze the shape of the cost function $I(\boldsymbol{\alpha})$ (equation 21) in the neighborhood

Table 2. Model parameters for carbonate-rich shale samples from the Eagle Ford Formation (EH5 and EV8) and clay-rich shale samples from the Haynesville Formation (HV35 and HH37).

	EH5	EV8	HV35	HH37		
κ	4.05	4.58	8.86	3.16	$\times 10^{-3}$	
λ	5.09	7.45	29.30	56.60	$\times 10^{-3}$	
μ_0	17.44	50.29	9.69	152.0	$\times 10^{6}$	MPa s
ζ	11.92	11.37	4.33	32.01	$\times 10^{3}$	
p_0	34.35	38.94	43.17	49.93		MPa

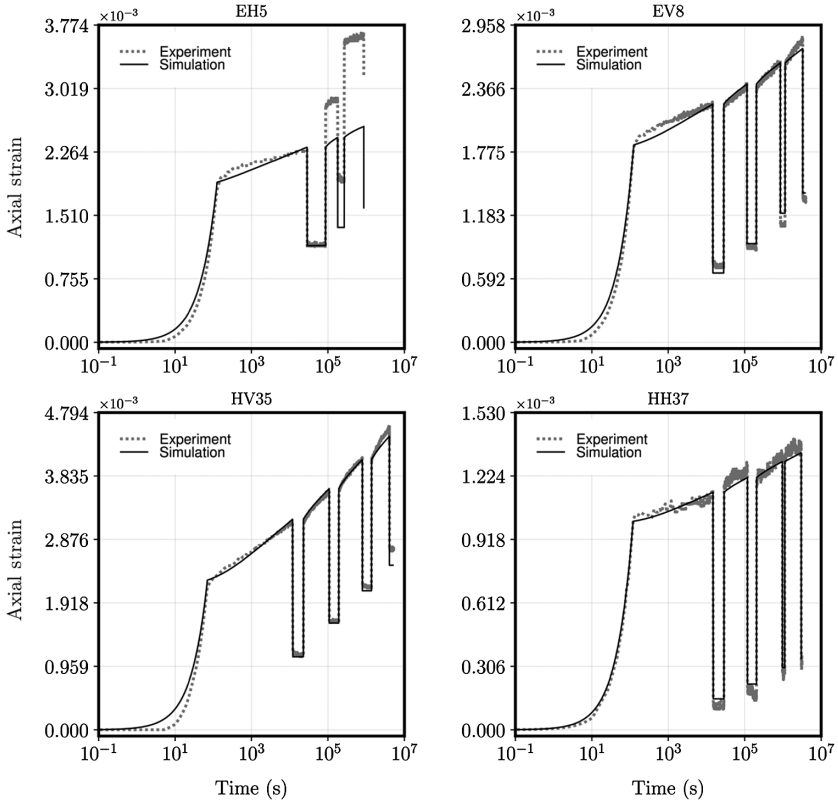

Figure 5. Comparison of axial strain from the laboratory experiments (the dotted gray lines) and the 3D finite-element simulation with implicit time integration of our viscoplastic model (the solid black lines) for all four samples: EH5 and EV8 are carbonate-rich shales from the Eagle Ford Formation and HV35 and HH37 are clay-rich shales from the Haynesville Formation. Simulation curves correspond to the optimized parameters obtained from minimizing the cost function in equation 21.

of the optimum (Appendix A). As a function of parameters κ, p_{y0}, μ_0, and ζ, the cost function exhibits a pronounced minimum, implying that a gradient-descent optimization procedure will quickly converge to the optimum value of those parameters. This is not the case, however, for parameter λ: the cost function is flat over a wide range of values — a behavior that indicates that the parameter is poorly constrained by the data (Appendix A). In our case, this is due to a lack of strain measurements in the *rate-independent* plastic deformation regime.

CONCLUSION

In this study, we propose a model for the time-dependent deformation (creep) of geomaterials under cyclic loading. Current modeling approaches rely on the imposition of a characteristic relaxation time, something that prevents their applicability to the case of loading cycles with disparate time scales. Here, we address this issue by developing a modeling framework that extends the well-known Cam-clay plasticity model to simulate creep through a Perzyna-type viscous deformation flow.

We validate the new viscoplastic model by simulating recent long-term and cyclic creep experiments on shale-rock samples, and we show that the new model reproduces the experimental results accurately. By using a gradient-descent training approach to minimize the discrepancy between experimental results and simulations, we find that the preconsolidation stress — reflecting the mechanical-state alteration of the rock samples as a result of drilling and underground retrieval operations — should be understood as a model parameter rather than a material parameter, and one that is subject to large variability and uncertainty.

An important aspect of the newly developed model is that it honors crucial properties such as positive energy dissipation during plastic and viscoplastic evolution and stress relaxation toward the yield surface. It also guarantees the stability of its implementation in finite-element codes of mechanical deformation, including an efficient return-mapping algorithm for the nonlinear iterations at each time step. Coupling with fluid flow is straightforward by using Biot poroelasticity in the elastic domain, and understanding stresses as effective stresses, $\boldsymbol{\sigma}' = \boldsymbol{\sigma} + bp_f\mathbf{1}$, where p_f is the fluid pressure and b is the Biot coefficient. The validation of our model as an effective stress model, however, would require dedicated additional experiments, in which the samples are saturated with fluid and loaded under different pore pressures. The water content of the samples that we worked with was small (1% for the Haynesville and 0.3% for the Eagle Ford samples), and the experiments were performed at ambient temperature. We are currently working on creep experiments at reservoir temperatures, and the results and the modeling will be reported in future work. An interesting extension of the model is consideration of anisotropy (in deformation and strength response) — a feature that is required for the accurate modeling of many geomaterials, including shales.

ACKNOWLEDGMENTS

Funding for this work was provided in part by Eni S.p.A. through the Coupled Flow and Reservoir Geomechanics: Computational Modeling of Induced Seismicity project. The laboratory data used here are contained in a published source (not a repository) cited in the references (Rassouli and Zoback, 2018).

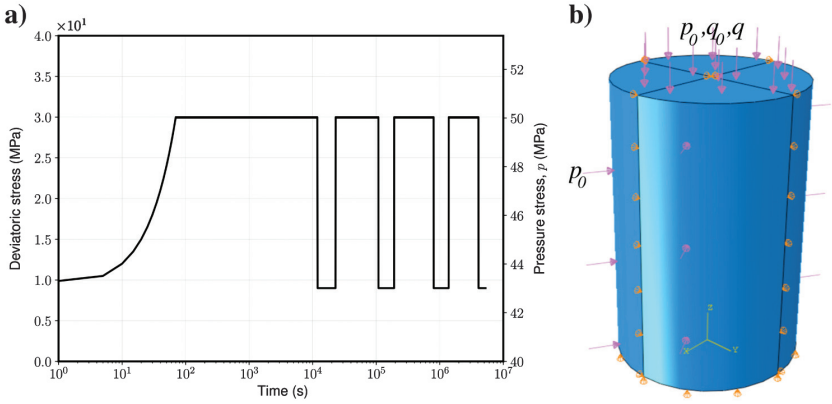

Figure A-1. (a) Stress loading function as a function of time for sample HV35, reproducing the four cycles of loading-creep-unloading-rebound (note the logarithmic time axis). (b) Schematic of the 3D finite-element simulation setup, reproducing the experimental conditions of the triaxial tests for sample HV35. The displacement in the z-direction is restrained at the bottom boundary, i.e., $u_z = 0$. The model is initialized with normal stress $p = 40$ MPa on the side boundary and $q_0 = 9$ MPa on the top boundary to replicate the experiment's initial stress state. Then, a cyclic load of $q = 21$ MPa is applied over time, as shown in (a). The experiments involve a constant state of stress; therefore, the number of elements does not play a role in these simulations — something that we have checked. Similarly, we use a sufficiently large number of time steps (1000 time steps per loading cycle) such that the results are independent of this choice.

DATA AND MATERIALS AVAILABILITY

Data associated with this research are available and can be obtained by contacting the corresponding author.

APPENDIX A

ADDITIONAL FIGURES AND TABLES

In this appendix, we provide additional details regarding the model application in a 3D finite-element method simulation (Figure A-1), sensitivity analysis (Figure A-2), parameter identification (Figure A-3), and evolution of the yield surface (Figure A-4). Finally, we also provide a summary of the model parameters for all of the shale samples that we studied (Table A-1).

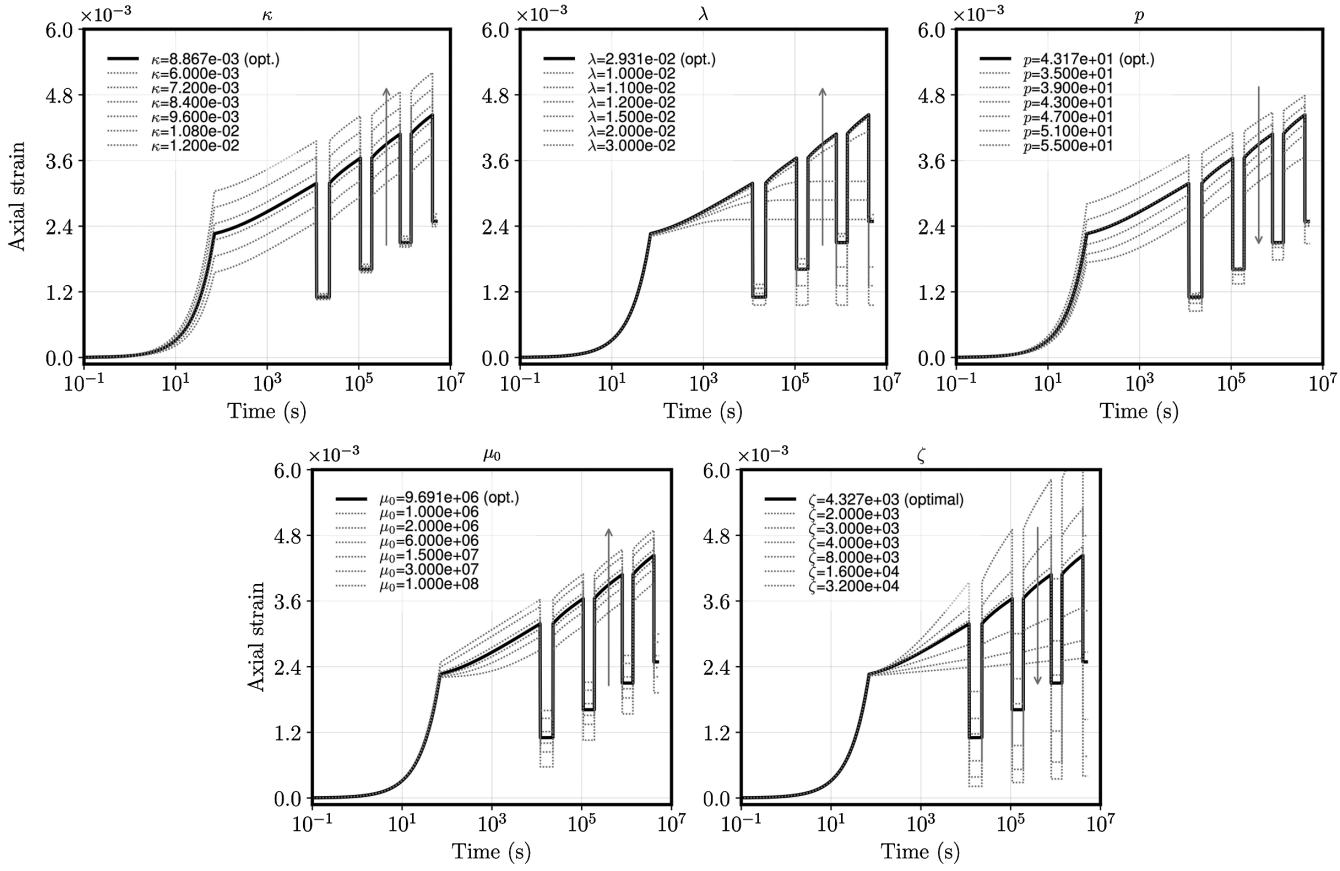

Figure A-2. Sensitivity of the modeled axial strain to parameters κ, λ, p_{y0}, μ_0, and ζ for sample HV35. The model response is obtained varying one parameter at a time, around the optimum parameter set obtained from gradient-descent optimization.

APPENDIX B

COMPARISON WITH A CLASSICAL MODEL OF VISCOPLASTICITY

It proves useful to contrast our proposed model with the classic Vermeer and Neher (1999) model of creep in rocks. In the latter model, the volumetric deformation is evaluated from classic soil mechanics concepts as

$$\dot{\varepsilon}_v^p = \frac{\mu/(1+e)}{t+\tau_c}\left(\frac{p_a}{p_y}\right)^{\frac{\lambda-\kappa}{\mu}}, \tag{B-1}$$

where μ and τ_c are the model parameters, p_a is defined as $p + q^2/(\eta_F^2 p)$ and, importantly, t is the time of creep deformation. It is worth noting that the number of creep parameters in our model (μ and ζ) is the same as in the Vermeer and Neher (1999) model (μ and τ_c). From equation B-1, the plastic multiplier $\dot{\gamma}$ and, therefore, the plastic strain tensor $\dot{\boldsymbol{\varepsilon}}^p$ are fully defined. The time variable t in this relation is difficult to reconcile with the theory of plasticity, where the stress difference from the yield surface drives the evolution of plastic deformations. In particular, for cyclic loading, it is unclear the point at which the reference for t should be set.

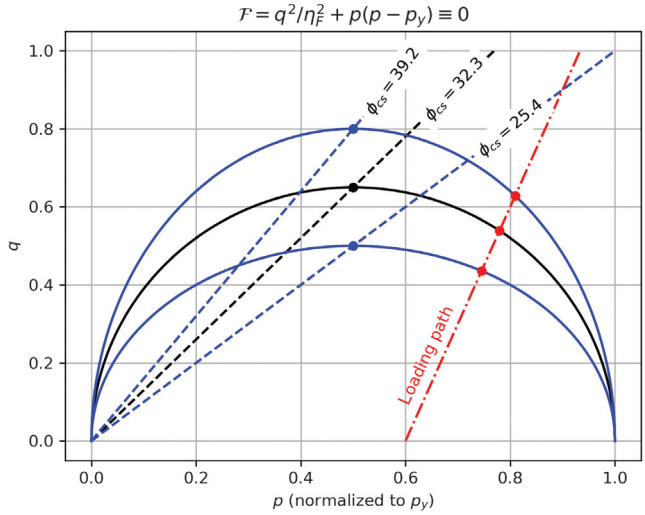

Figure A-4. Evolution of the yield surface for $\eta_F = 1.0$, 1.3, and 1.6 associated to CSL angles $\phi_{cs} = 25.4^\circ$, 32.2°, and 39.2°, respectively. As can be seen here, the unit normal to the yield surfaces at the intersection with the triaxial loading path from our experiments does not vary significantly. This leads us to suspect that the choice of η_F does not significantly change our inference of the other model parameters.

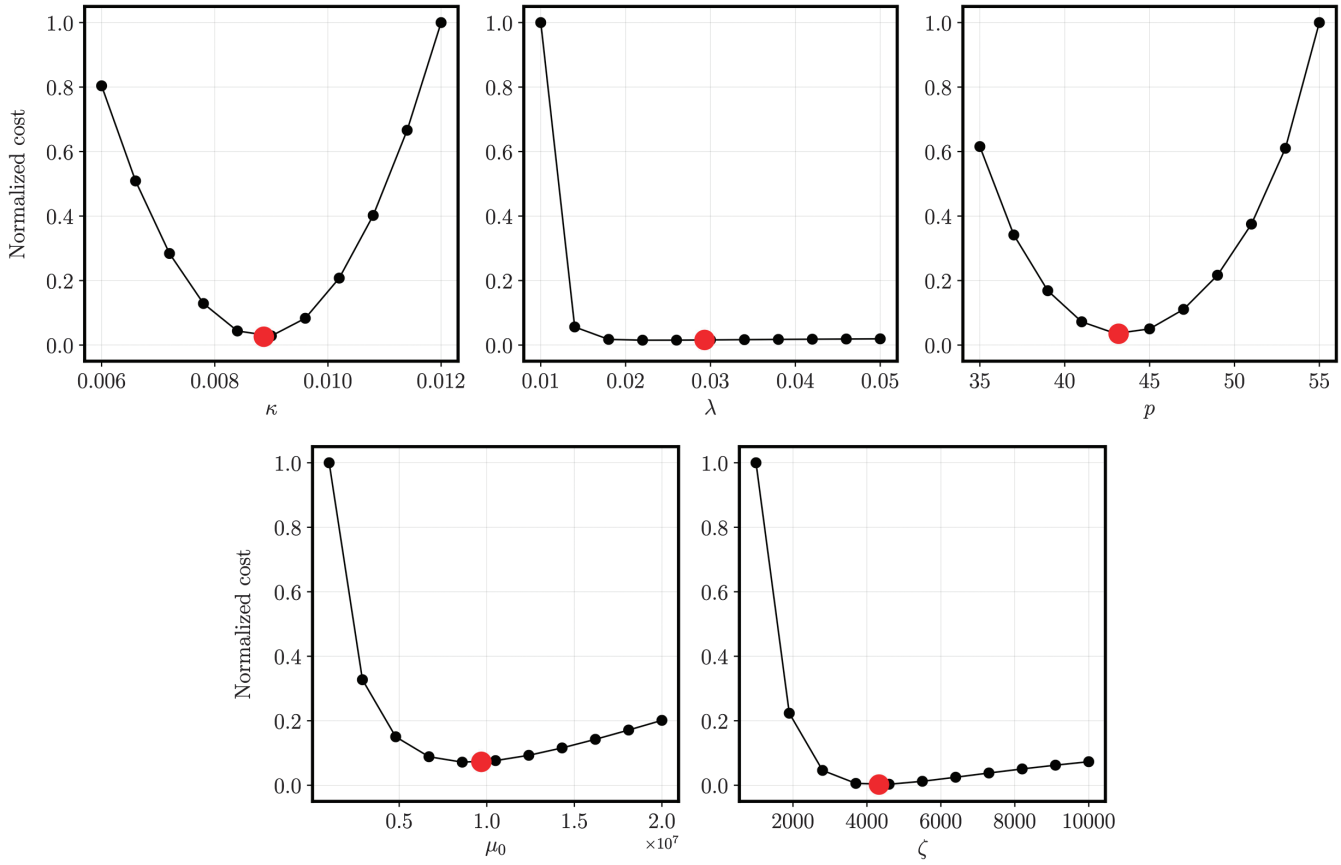

Figure A-3. Sensitivity of the cost function used in the optimization to parameters κ, λ, p_{y0}, μ_0, and ζ for sample HV35. The cost function is evaluated by varying one parameter at a time, around the optimum parameter set obtained from gradient-descent optimization. As function of parameters κ, p_{y0}, μ_0, and ζ, the cost function exhibits a pronounced minimum, implying that a gradient-descent optimization procedure will quickly converge to the optimum value of those parameters. This is not the case, however, for parameter λ: The cost function is flat over a wide range of values — a behavior that indicates that the parameter is poorly constrained by the data, and results in relatively slow convergence (typically 100–200 iterations) of the gradient-descent algorithm. In this case, this is due to a lack of strain measurements in the *rate-independent* plastic deformation regime.

To validate our implementation of the Vermeer and Neher (1999) model, we use the undrained problem reported in their work (Vermeer and Neher, 1999). The material parameters are taken as $\nu = 0.25$, $\kappa = 0.025$, $\lambda = 0.1575$, $\phi_{cs} = 32^{\circ}$, $\mu = 0.006$, and $\tau_c = 24$ h, assuming an initial void ratio of $e_0 = 0.5$. The results of undrained axial loading (Figure B-1) precisely match those reported in Vermeer and Neher (1999).

To further test the models, we simulate an uniaxial compression test subject to an initial stress of $p_0 = 373$ kPa and a deviatoric stress $q = 500$ kPa. The axial load q is increased linearly within 1 day and kept fixed for 9 days. Because this is a stress-controlled experiment, we take the final displacement from Vermeer's model as the reference curve and evaluate parameters of our proposed model using the optimization technique described in the main manuscript, leading to parameter values $\kappa = 0.039$, $\lambda = 0.251$, $\mu = 6.45 \times 10^4$, $\zeta = 135.7$, and $p_{y0} = 448$ kPa. Because the plastic deformation mechanism is different for each model, the parameters providing a best match (Figure B-2) are also different.

In Figure B-3, we plot the evolution of p_a and p_y as well as $\mathcal{F} = p_a - p_y$. After a sufficiently long time, the system should reach a new equilibrium with a new preconsolidation stress and yield surface satisfying the new stress state. This is indeed the case

Table A-1. Model parameters for carbonate-rich shale samples from the Eagle Ford Formation (EH5 and EV8) and clay-rich shale samples from the Haynesville Formation (HV35 and HH37) for different values of the critical-state parameter $\eta_F = 1.0$, 1.3, and 1.6.

η_F		EH5	EV8	HV35	HH37		
1.00	κ	4.05	4.33	8.75	3.06	$\times 10^{-3}$	
	λ	5.09	7.09	22.35	56.72	$\times 10^{-3}$	
	μ_0	17.44	57.0	3.94	152.1	$\times 10^{6}$	MPa s
	ζ	11.92	14.66	6.61	35.65	$\times 10^{3}$	
	p_0	34.35	39.38	46.33	50.95		MPa
1.30	κ	4.05	4.58	8.86	3.16	$\times 10^{-3}$	
	λ	5.09	7.45	29.30	56.60	$\times 10^{-3}$	
	μ_0	17.44	50.29	9.69	152.0	$\times 10^{6}$	MPa s
	ζ	11.92	11.37	4.33	32.01	$\times 10^{3}$	
	p_0	34.35	38.94	43.17	49.93		MPa
1.60	κ	3.81	4.60	8.77	3.16	$\times 10^{-3}$	
	λ	5.16	7.80	22.44	56.60	$\times 10^{-3}$	
	μ_0	7.20	84.15	3.51	152.0	$\times 10^{6}$	MPa s
	ζ	7.64	8.30	3.35	31.59	$\times 10^{3}$	
	p_0	31.67	38.11	43.22	49.60		MPa

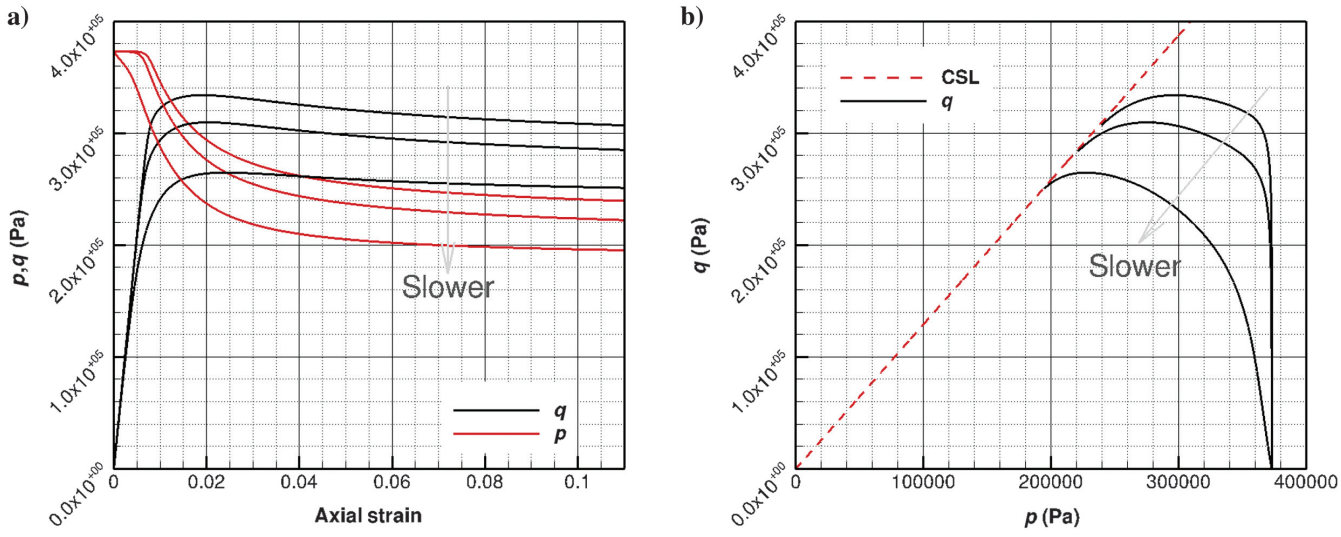

Figure B-1. Results from the simulation reported in Vermeer and Neher (1999) for modeling viscoplastic deformation under undrained loading conditions (i.e., $\varepsilon_v = 0$ or $\varepsilon_{22} = \varepsilon_{33} = -\varepsilon_{11}/2$) for axial strain rates of 0.00094%/min, 0.15%/min, and 1.1%/min. (a) Evolution of p and q versus axial strain. (b) Evolution of stresses in the p-q space.

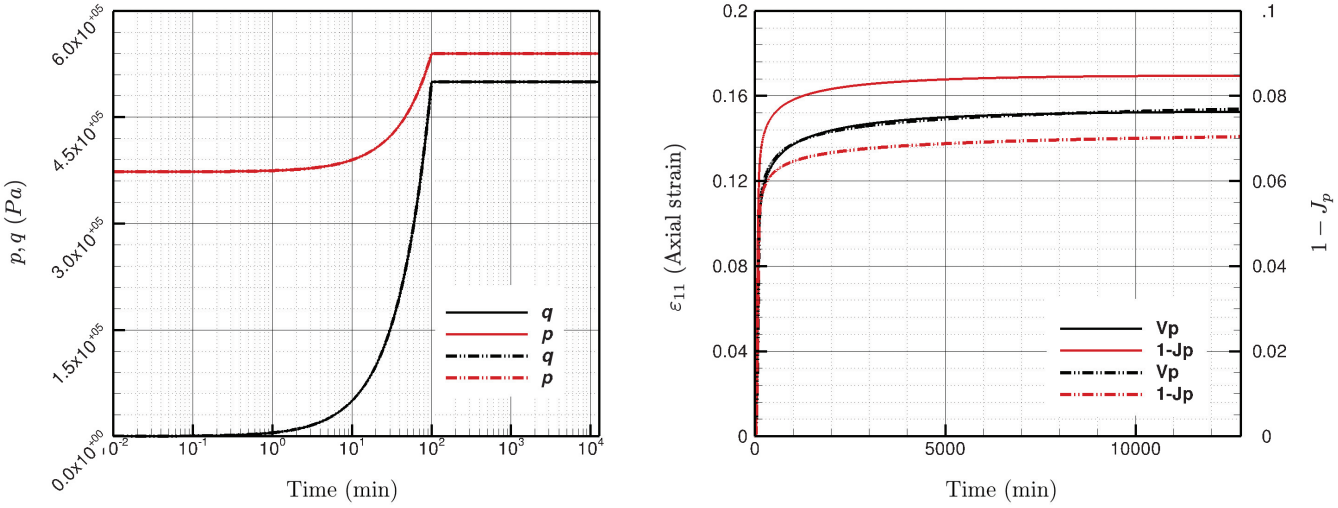

Figure B-2. Uniaxial compression test with initial confining pressure of 373 kPa and deviatoric stress of $q = 500$ kPa applied in 1 day and kept fixed for 500 days. The solid lines indicate our proposed model, and the dashed-dotted lines represent the Vermeer and Neher (1999) model.

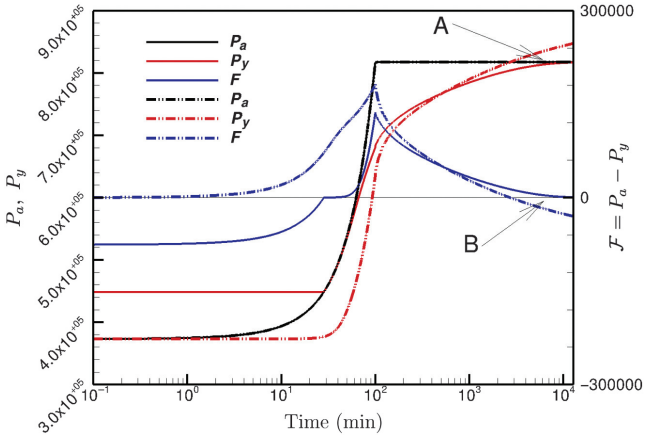

Figure B-3. Evolution of $p_a = p + q^2/(\eta_F^2 p)$, p_y, and $\mathcal{F} = p_a - p_y$ as a function of time. The solid lines indicate results from our proposed model, and the dashed-dotted lines represent the Vermeer and Neher (1999) model.

for our viscoplastic model: the yield surface grows and becomes tangent to the applied active stress (point A), indicating a proper dissipation of the excess stresses through time-dependent plastic deformation. This behavior implies that the yield function $\mathcal{F}$ becomes positive initially and then asymptotes back to zero (point B), illustrating the behavior of a Perzyna-type model. In contrast, the Vermeer model predicts an evolution in which the yield surface overshoots the applied active stress — a thermodynamically incompatible stress state.

REFERENCES

Aagaard, B. T., M. G. Knepley, and C. A. Williams, 2013, A domain decomposition approach to implementing fault slip in finite-element models of quasi-static and dynamic crustal deformation: Journal of Geophysical Research: Solid Earth, **118**, 3059–3079, doi: 10.1002/jgrb.50217.

Adachi, T., and F. Oka, 1982, Constitutive equations for normally consolidated clay based on elasto-viscoplasticity: Soils and Foundations, **22**, 57–70, doi: 10.3208/sandf1972.22.4_57.

Amitrano, D., and A. Helmstetter, 2006, Brittle creep, damage, and time to failure in rocks: Journal of Geophysical Research: Solid Earth, **111**, B11201, doi: 10.1029/2005JB004252.

Borja, R. I., 2013, Plasticity: Modeling and computation: Springer.

Borja, R. I., and J. Choo, 2016, Cam-Clay plasticity — Part 8: A constitutive framework for porous materials with evolving internal structure: Computer Methods in Applied Mechanics and Engineering, **309**, 653–679, doi: 10.1016/j.cma.2016.06.016.

Borja, R. I., and E. Kavazanjian, 1985, A constitutive model for the stress–strain–time behaviour of 'wet' clays: Geotechnique, **35**, 283–298, doi: 10.1680/geot.1985.35.3.283.

Borja, R. I., C. Tamagnini, and A. Amorosi, 1997, Coupling plasticity and energy-conserving elasticity models for clays: Journal of Geotechnical and Geoenvironmental Engineering, **123**, 948–957, doi: 10.1061/(ASCE)1090-0241(1997)123:10(948).

Brantut, N., P. Baud, M. Heap, and P. Meredith, 2012, Micromechanics of brittle creep in rocks: Journal of Geophysical Research: Solid Earth, **117**, B08412, doi: 10.1029/2011JB008730.

Braun, J., C. Thieulot, P. Fullsack, M. DeKool, C. Beaumont, and R. Huismans, 2008, DOUAR: A new three-dimensional creeping flow numerical model for the solution of geological problems: Physics of the Earth and Planetary Interiors, **171**, 76–91, doi: 10.1016/j.pepi.2008.05.003.

Cao, Y., J. Deng, B. Yu, Q. Tan, and C. Ma, 2014, Analysis of sandstone creep and wellbore instability prevention: Journal of Natural Gas Science and Engineering, **19**, 237–243, doi: 10.1016/j.jngse.2014.05.013.

Carter, N. L., D. A. Anderson, F. D. Hansen, and R. L. Kranz, 1981, Creep and creep rupture of granitic rocks: Geophysical Monographs, **24**, 61–82, doi: 10.1029/GM024p0061.

Castelnau, O., D. Blackman, R. Lebensohn, and P. Ponte Castañeda, 2008, Micromechanical modeling of the viscoplastic behavior of olivine: Journal of Geophysical Research: Solid Earth, **113**, B09202, doi: 10.1029/2007JB005444.

Chang, C., and M. D. Zoback, 2010, Viscous creep in room-dried unconsolidated Gulf of Mexico shale — 2: Development of a viscoplasticity model: Journal of Petroleum Science and Engineering, **72**, 50–55, doi: 10.1016/j.petrol.2010.03.002.

Coussy, O., 1995, Mechanics of porous continua: Wiley.

De Waal, J., and R. Smits, 1988, Prediction of reservoir compaction and surface subsidence: Field application of a new model: SPE Formation Evaluation, **3**, 347–356, doi: 10.2118/14214-PA.

Dudley, J., M. T. Myers, R. D. Shew, and M. M. Arasteh, 1998, Measuring compaction and compressibilities in unconsolidated reservoir materials by time-scaling creep: SPE Reservoir Evaluation & Engineering, **1**, 430–437, doi: 10.2118/51324-PA.

Finnie, I., and W. R. Heller, 1959, Creep of engineering materials: McGraw-Hill.

Geng, Z., A. Bonnelye, M. Chen, Y. Jin, P. Dick, C. David, X. Fang, and A. Schubnel, 2017, Elastic anisotropy reversal during brittle creep in shale: Geophysical Research Letters, **44**, 10,887–10,895, doi: 10.1002/grl.v44.21.

Glerum, A., C. Thieulot, M. Fraters, C. Blom, and W. Spakman, 2018, Nonlinear viscoplasticity in ASPECT: Benchmarking and applications to subduction: Solid Earth, **9**, 267–294, doi: 10.5194/se-9-267-2018.

Grgic, D., and D. Amitrano, 2009, Creep of a porous rock and associated acoustic emission under different hydrous conditions: Journal of Geophysical Research: Solid Earth, **114**, B10201, doi: 10.1029/2006JB004881.
Hagin, P. N., and M. D. Zoback, 2004a, Viscous deformation of unconsolidated reservoir sands — Part 1: Time-dependent deformation, frequency dispersion, and attenuation: Geophysics, **69**, 742–751, doi: 10.1190/1.1759460.
Hagin, P. N., and M. D. Zoback, 2004b, Viscous deformation of unconsolidated reservoir sands — Part 2: Linear viscoelastic models: Geophysics, **69**, 742–751, doi: 10.1190/1.1759460.
Hao, S.-W., B.-J. Zhang, J.-F. Tian, and D. Elsworth, 2014, Predicting time-to-failure in rock extrapolated from secondary creep: Journal of Geophysical Research: Solid Earth, **119**, 1942–1953, doi: 10.1002/2013JB010778.
Heap, M., P. Baud, P. Meredith, S. Vinciguerra, A. Bell, and I. Main, 2011, Brittle creep in basalt and its application to time-dependent volcano deformation: Earth and Planetary Science Letters, **307**, 71–82, doi: 10.1016/j.epsl.2011.04.035.
Houlsby, G., 1985, The use of a variable shear modulus in elastic-plastic models for clays: Computers and Geotechnics, **1**, 3–13, doi: 10.1016/0266-352X(85)90012-6.
Jha, B., and R. Juanes, 2014, Coupled multiphase flow and poromechanics: A computational model of pore pressure effects on fault slip and earthquake triggering: Water Resources Research, **50**, 3776–3808, doi: 10.1002/2013WR015175.
Kimoto, S., F. Oka, and Y. Higo, 2004, Strain localization analysis of elasto-viscoplastic soil considering structural degradation: Computer Methods in Applied Mechanics and Engineering, **193**, 2845–2866, doi: 10.1016/j.cma.2003.09.017.
Kutter, B., and N. Sathialingam, 1992, Elastic-viscoplastic modelling of the rate-dependent behaviour of clays: Géotechnique, **42**, 427–441, doi: 10.1680/geot.1992.42.3.427.
Leong, W., and J. Chu, 2002, Effect of undrained creep on instability behaviour of loose sand: Canadian Geotechnical Journal, **39**, 1399–1405, doi: 10.1139/t02-076.
Lewis, R. W., A. Makurat, and W. K. Pao, 2003, Fully coupled modeling of seabed subsidence and reservoir compaction of North Sea oil fields: Hydrogeology Journal, **11**, 142–161, doi: 10.1007/s10040-002-0239-z.
Lubliner, J., 1990, Plasticity theory: Macmillan Publishing Company (reprinted with corrections, Dover, New York, 2008).
Marsden, J. E., and T. J. R. Hughes, 1983, Mathematical foundations of elasticity: Prentice-Hall (reprinted with corrections, Dover, New York, 1994).
Mavko, G., and N. Saxena, 2016, Rock-physics models for heterogeneous creeping rocks and viscous fluids: Geophysics, **81**, no. 4, D427–D440, doi: 10.1190/geo2015-0531.1.
Nakken, S., T. Christensen, R. Marsden, and R. Holt, 1989, Mechanical behaviour of clays at high stress levels for well bore stability applications: ISRM International Symposium, International Society for Rock Mechanics, ISRM-IS-1989-018.
Niemunis, A., and I. Herle, 1997, Hypoplastic model for cohesionless soils with elastic strain range: Mechanics of Cohesive-frictional Materials, **2**, 279–299, doi: 10.1002/(SICI)1099-1484(199710)2:4<279::AID-CFM29>3.0.CO;2-8.
Perzyna, P., 1966, Fundamental problems in viscoplasticity: Advances in Applied Mechanics, **9**, 243–377, doi: 10.1016/S0065-2156(08)70009-7.
Pietruszczak, S., 2010, Fundamentals of plasticity in geomechanics: CRC Press.
Rassouli, F. S., and M. D. Zoback, 2018, Comparison of short-term and long-term creep experiments in shales and carbonates from unconventional gas reservoirs: Rock Mechanics and Rock Engineering, **51**, 1995–2014, doi: 10.1007/s00603-018-1444-y.
Reber, J. E., N. W. Hayman, and L. L. Lavier, 2014, Stick-slip and creep behavior in lubricated granular material: Insights into the brittle-ductile transition: Geophysical Research Letters, **41**, 3471–3477, doi: 10.1002/2014GL059832.
Revil, A., 1999, Pervasive pressure-solution transfer: A poro-visco-plastic model: Geophysical Research Letters, **26**, 255–258, doi: 10.1029/1998GL900268.
Roscoe, K., and J. Burland, 1968, On the generalized stress-strain behaviour of wet clay, *in* J. Heyman and F. A. Leckie, eds., Engineering plasticity: Cambridge University Press, 535–609.
Rundle, J., and D. Jackson, 1977, A three-dimensional viscoelastic model of a strike slip fault: Geophysical Journal of the Royal Astronomical Society, **49**, 575–591, doi: 10.1111/j.1365-246X.1977.tb01305.x.
Rutqvist, J., J. Birkholzer, and C.-F. Tsang, 2008, Coupled reservoir-geomechanical analysis of the potential for tensile and shear failure associated with CO_2 injection in multilayered reservoir-caprock systems: International Journal of Rock Mechanics and Mining Sciences, **45**, 132–143, doi: 10.1016/j.ijrmms.2007.04.006.
Scholz, C., 1968, Mechanism of creep in brittle rock: Journal of Geophysical Research, **73**, 3295–3302, doi: 10.1029/JB073i010p03295.
Segura, J., and I. Carol, 2008, Coupled HM analysis using zero-thickness interface elements with double nodes — Part 1: Theoretical model: International Journal for Numerical and Analytical Methods in Geomechanics, **32**, 2083–2101, doi: 10.1002/nag.v32:18.
Settari, A., and F. Mourits, 1998, A coupled reservoir and geomechanical simulation system: SPE Journal, **3**, 219–226, doi: 10.2118/50939-PA.
Shao, J.-F., Q.-Z. Zhu, and K. Su, 2003, Modeling of creep in rock materials in terms of material degradation: Computers and Geotechnics, **30**, 549–555, doi: 10.1016/S0266-352X(03)00063-6.
Simo, J., and T. J. Hughes, 1998, Computational inelasticity: Springer-Verlag.
Simo, J., and M. Ortiz, 1985, A unified approach to finite deformation elastoplastic analysis based on the use of hyperelastic constitutive equations: Computer Methods in Applied Mechanics and Engineering, **49**, 221–245, doi: 10.1016/0045-7825(85)90061-1.
Simulia, 2018, Abaqus user's manual, version 6.14: Simulia.
Sone, H., and M. D. Zoback, 2013a, Mechanical properties of shale-gas reservoir rocks — Part 1: Static and dynamic elastic properties and anisotropy: Geophysics, **78**, no. 5, D381–D392, doi: 10.1190/geo2013-0050.1.
Sone, H., and M. D. Zoback, 2013b, Mechanical properties of shale-gas reservoir rocks — Part 2: Ductile creep, brittle strength, and their relation to the elastic modulus: Geophysics, **78**, no. 5, D393–D402, doi: 10.1190/geo2013-0051.1.
Sone, H., and M. D. Zoback, 2014, Time-dependent deformation of shale gas reservoir rocks and its long-term effect on the in situ state of stress: International Journal of Rock Mechanics and Mining Sciences, **69**, 120–132, doi: 10.1016/j.ijrmms.2014.04.002.
Thomas, L., L. Chin, R. Pierson, and J. Sylte, 2003, Coupled geomechanics and reservoir simulation: SPE Journal, **8**, 350–358, doi: 10.2118/87339-PA.
Truesdell, C., and R. A. Toupin, 1960, The classical field theories, *in* S. Flügge, ed., Principles of classical mechanics and field theory: Springer-Verlag, volume III/1 of Handbuch der Physik, 226–793.
Tutuncu, A. N., A. L. Podio, and M. M. Sharma, 1998, Nonlinear viscoelastic behavior of sedimentary rocks — Part 2: Hysteresis effects and influence of type of fluid on elastic moduli: Geophysics, **63**, 195–203, doi: 10.1190/1.1444313.
Vermeer, P., and H. Neher, 1999, A soft soil model that accounts for creep: Proceedings of Symposium "Beyond 2000 in Computational Geotechnics", 249–261.
Wang, W., L. Sluys, and R. De Borst, 1997, Viscoplasticity for instabilities due to strain softening and strain-rate softening: International Journal for Numerical Methods in Engineering, **40**, 3839–3864, doi: 10.1002/(SICI)1097-0207(19971030)40:203.0.CO;2-6.
Wood, D. M., 1990, Soil behaviour and critical state soil mechanics: Cambridge University Press.
Yang, X.-S., 2000, Nonlinear viscoelastic compaction in sedimentary basins: Nonlinear Processes in Geophysics, **7**, 1–8, doi: 10.5194/npg-7-1-2000.
Yang, X.-S., 2002, A mathematical model for voigt poro-visco-plastic deformation: Geophysical Research Letters, **29**, 10, doi: 10.1029/2001GL014014.
Yin, Z.-Y., C. S. Chang, M. Karstunen, and P.-Y. Hicher, 2010, An anisotropic elastic-viscoplastic model for soft clays: International Journal of Solids and Structures, **47**, 665–677, doi: 10.1016/j.ijsolstr.2009.11.004.
Zytynski, M., M. Randolph, R. Nova, and C. Wroth, 1978, On modelling the unloading-reloading behaviour of soils: International Journal for Numerical and Analytical Methods in Geomechanics, **2**, 87–93, doi: 10.1002/nag.1610020107.